

Development of Novel and Cost Effective Corrosion and Erosion Resistant Coatings for High Temperature Geothermal Applications: Geo-Coat

Francesco Fanicchia¹, Namrata Kale¹, Shiladitya Paul¹, Raja Khan¹, Sandeep Irukuvarghula¹, Emily Davison¹, Josh Barras¹, Catherine Leahy¹, Henry Begg¹, Douglas Watson², Alastair Pearson², Frazer Brownlie^{2,*}, Trevor Hodgkiess², Sæmundur Guðlaugsson³, Sigrún N. Karlsdóttir⁴, Gifty B. Oppong⁴, Danyil Kovalov⁴, Ioana Csaki⁵, Laura E. Geambazu⁵, Sunna Ó. Wallevik⁶, Jan Prikryl⁶, Kristján F. Alexandersson⁶, Fahim Chowdhury⁷, Hye Chowdhury, Vlad Motoiu⁸, Petra Motoiu⁸, Per Kjellgren⁹, Aurelian Buzaiianu¹⁰, Anghel Ioncea¹⁰, Kolbrún R. Ragnarsdóttir¹¹, Kristján Leósson¹¹, Dagur I. Ólafsson¹¹, Helen Ó. Haraldsdóttir¹¹

¹TWI Ltd, Cambridge, United Kingdom

²Weir Group PLC (The), Glasgow, United Kingdom

³Orkuveita Reykjavíkur SF, Reykjavik, Iceland

⁴University of Iceland, Reykjavik, Iceland

⁵University "Politehnica" Bucharest, Bucharest, Romania

⁶Gerosion Ehf, Reykjavik, Iceland

⁷Technovative Solutions Ltd, Manchester, United Kingdom

⁸Tehnoid Com Srl, Bucharest, Romania

⁹Flowphys AS, Oslo, Norway

¹⁰Metav –Cercetare Dezvoltare Srl, Bucharest, Romania

¹¹Nyskopunarmidstod Islands, Reykjavik, Iceland

*University of Strathclyde, Glasgow, UK

Francesco.Fanicchia@twi.co.uk

Keywords: Coatings, Corrosion, Erosion, Geothermal Environment, Geo-Coat

ABSTRACT

Geothermal sources are aggressive natural environments and thus the utilization of these sources can lead to compromised integrity of various components of geothermal power plants including liners and well casings, well heads, turbines, etc. Dissolved CO₂, H₂S, NH₃ gases, sulphate and chloride ions are the dominant species generating corrosion, heavily dependent on operational factors such as the pressure, temperature, flow rate, oxygen concentration, suspended solids, flow regime and pH level of the geothermal fluid. The materials currently used are either not always capable of performing in such harsh environments thus leading to a constant need for maintenance (e.g. carbon steel), or highly expensive (e.g. Ni-/Ti-based alloys). Therefore, the geothermal industry needs to improve plant capability to withstand this harsh environment, to maintain the equipment longevity and generation efficiency. Additionally, there is the requirement to produce better geothermal power plant equipment protection design concepts through virtual prototyping to meet the increasing requirements for lifecycle costs, environmental impacts and end-of-life considerations. To this aim, the scope of the Geo-Coat project is threefold: (a) to develop and test in geothermal environments specialised corrosion-, scaling- and erosion-resistant coatings and bulk materials, based on selected high-entropy alloys, ceramic/metal mixtures, nickel-phosphorous-polytetrafluoroethylene and metal matrix composites to be applied through thermal powder coating techniques (high velocity oxygen fuel spray, laser metal deposition, electrospark deposition, electroless plating and hot isostatic pressing) (b) to develop a multi-phase, multi-component, high-temperature and high-pressure fluid flow simulator software including corrosion, erosion and scaling formation models and (c) to integrate the simulator and the coatings experimental results, to provide a powerful decision-based system for geothermal power plant operators. Preliminary results demonstrated promising corrosion and tribological performances for some of the tested materials in lab-based simulated geothermal environments.

1. INTRODUCTION

Components of geothermal power plants are often damaged by a combination of corrosion, erosion and scaling mechanisms, the extent of which depends on the geothermal fluid chemistry, its thermodynamic properties and the component material. Corrosion in these environments is generally linked to geothermal fluid pH, temperature, pressure, flow and concentration of non-condensable gases (e.g. H₂S, CO₂) and chloride ions [1]. The main forms of observed corrosion, in general, are uniform corrosion and localized corrosion (e.g. pitting and crevice corrosion) [2, 3, 4]. However, other forms of corrosion such as Environmental Assisted Cracking (EAC) including Hydrogen Embrittlement (HE), Hydrogen Induced Cracking (HIC), Stress Corrosion Cracking (SCC), Corrosion Fatigue Cracking (CFC) and Sulfide Stress Cracking (SSC) can also occur [5]. Typical components affected by uniform corrosion are well casing pipes and fluid transportation pipes in contact with hot acidic fluid while pitting and crevice corrosion, generally enhanced in the presence of chloride and sulphate ions, are critical in heat exchanger components due to their thin walls. Erosion-corrosion is activated when there is relative movement between the geothermal fluid and the base metal [1]. The mechanical action of the particles suspended in the fluid continuously exposes fresh metal surface to the corrosive fluid, thus accelerating the process. Erosion-corrosion is enhanced in areas of localized high flow, such as at pipelines elbows, turbines and tube constrictions. Finally, scaling (in the form of silica and silicates, carbonates and sulphides compounds) occur due to either an increase in silica concentration or a sudden drop in geothermal fluid temperature. Scaling is a common issue encountered in turbines and heat exchanger components. The occurrence of one (or more) of the above degradation mechanisms leads to the affected component(s) not being able to fulfil

their role and the need for, sometimes unscheduled, maintenance operations [6, 7, 8]. Component damage therefore affects the overall plant operation reliability, with adverse consequences on energy production and therefore profitability. Minimization or even eradication of these occurrences can therefore reduce the need for frequent maintenance and subsequently the cost of operation.

Carbon steel is the desired structural material for geothermal applications, primarily due to its low cost, good availability and weldability. However, its reduced resistance to corrosion and erosion-corrosion at several locations within the geothermal power plant, has stimulated the development of environmentally heavy and expensive corrosion resistant alloys such as nickel- and titanium-based [9]. Considerable savings in both environmental load and material cost could thus be achieved if it were possible to replace the corrosion-resistant alloys with carbon steel coated with high-performance erosion, corrosion and scaling resistant layers in the areas in contact with the geothermal fluid. Available literature on coatings for geothermal applications is rather scarce. Early studies focused on the use of non-metallic materials such as organic coatings. An example of this application is the work of Jacobson et al., [10] where a range of commercial organic coatings and lining materials have been tested in the Magnamax 1 Salton Sea brine. Among the tested coatings, Teflon PFA was deemed suitable for service, although bonding issues with carbon steel were raised. A range of polymeric materials were also screened by Lorensen et al., [11], who evaluated weight change and scale stability with time for temperatures up to 300°C and in erosion tests. Results showed a survival time of up to 1300h for several materials including fluorocarbon and unhydrolyzable aromatic or cross-linked aliphatic polymers and best performance in erosion tests for epoxy based resins and fluorocarbons. The use of thermal spray as coating deposition technique has also been evaluated by some research studies. It is known, for instance, that carbon steel structures suffering severe hydrogen sulphide exposure in Italian geothermal plants are protected by flame sprayed zinc coatings combined with phenolic oil base paints [12]. An interesting application of plasma spray by Maden [13] showed how a combination of plasma sprayed stainless steel impregnated with an air-sprayed water-based dispersion of PTFE is able to produce a system with low surface tension and low friction characteristics. More recently, Csaki et al., [14] evaluated the behavior of a high-velocity oxygen fuel sprayed (HVOF) NiCrBSi coating sprayed on a carbon steel plate in adhesion, wear resistance and exposure to geothermal steam. The study showed promising results for the coated system in terms of mechanical properties, although the layer was not deemed adequate as a barrier to corrosion. A comprehensive review of coatings for geothermal applications is reported in [15]. These studies demonstrate that coatings could in principle represent a real economically- and environmentally-viable solution to tackle the harsh conditions experienced by components within a geothermal power plant. However, in order for these systems to be reliably employed in geothermal plants, new coatings must be developed with remarkable capabilities in terms of corrosion, erosion and scaling resistance.

The aim of the Geo-Coat project is thus to develop novel corrosion, erosion and scaling coatings and bulk materials based on high-entropy alloys (HEA), ceramic/metal mixtures (cermets), nickel-phosphorous-polytetrafluoroethylene (PTFE) coatings and Metal Matrix Composites (MMC) materials produced through high velocity oxygen fuel spray (HVOF), Laser cladding (LC), Electrospray deposition (ESD) and Electroless plating (ENP) and Hot Isostatic Pressing (HIP). The systems produced were tested in two phases: (a) a lab-based testing stage performed in simulated geothermal conditions and (b) a testing stage in real geothermal conditions performed at the Hellisheiði power plant (Reykjavik, Iceland). This paper reports the findings from the first stage of tests, where linear polarization resistance and Tafel scan were employed to evaluate the corrosion resistance properties and erosion wear and contact angle tests were employed to evaluate the tribological performances. The systems performance was compared to standard wrought materials currently employed for geothermal plant components (i.e. pipelines and casing, turbine, heat exchangers). The materials selected as coating substrates represent an economical version of the comparison wrought alloys tested and thus are generally less corrosion and erosion resistant. By this, the aim is to demonstrate, for the tested coatings, similar or better performance compared to the state-of-the-art materials, both in terms of corrosion-erosion and cost. In parallel to the experimental coating development work, a multi-phase, multi-component, high-temperature and high-pressure Flow Assurance Simulator (FAS) software including corrosion, erosion and scaling formation is generated. The simulator can be employed in combination with experimental coating data in order to provide power plant operators with damage predicting capability and coating solutions on a case-specific basis.

2. MATERIALS AND METHODOLOGY

Materials and Setup

Five custom-made HEA powders, belonging to three composition classes, were employed as starting materials for coatings produced through HVOF, LC and ESD deposition and produced through either mechanical alloying or gas atomisation: CoCrFeMo_xNi (HEA1 and HEA2), Co_xCrFeMoNi (HEA3 and HEA4) and Al_xCoCrFeNi (HEA5). The same powders were employed, high-pressure sintered and heat treated, to produce rods for ESD deposition. For HVOF deposition, three commercial Cermet powders were also employed (Oerlikon-Metco): Amdry 5843 (WC-Co-Cr, CA1), Amdry 5260 (Cr₃C₂-NiCr, CA2) and Diamalloy 2001 (Ni-Cr-Fe-Si-B-C, CA3). In this way, a total of eight powders were produced (Figure 2). Bulk MMCs were produced by HIP starting from different commercial powders: AGA IN625 (LPW, UK), and Ti-6Al-4V (LPW, UK) used as matrix phase, and SiC, Si₃N₄ and TiB₂ (Reade Advanced Materials, USA) used as filler materials. Several solution reagents were employed to produce Ni-P-PTFE coatings via electroless technique, including a nickel and PTFE source, reducing and complexing agents, accelerator, surfactant, and pH regulator. The produced coatings and bulk were deposited onto four different substrate alloy types: S1-S235JR (E235B), S2-316 (X5CrNiMo17-12-2), S3 alloy 2767 (45NiCrMoV16-6) and S4-304L (X2CrNi19-11). The performance of coated substrates and bulk MMCs were compared against state-of-the-art (uncoated) materials, representing alloy compositions currently employed in geothermal power plant components: S1-P265GH (DIN17155 HII), S2-630 (X5CrNiCuNb16-4), S3-A470 grade C, S4-304L (X2CrNi19-11), S5-Ti-6Al-4V, S5-Inconel 625 (UNS N06625) and S6-254 SMO (X1CrNiMoCuN20-18-7). The coating substrates were selected as a more economical alternative to the state-of-the-art materials, with the aim of maintaining comparable (or better) corrosion, erosion and scaling performances at a lower cost with the coated systems. For the HVOF depositions, the Metco® DJ9HA torch was employed as deposition equipment while a Trumpf Trudisk 8002 5.3 kW disc laser system equipped with a TruControl 1000 controller and Trumpf BEO D70 processing optics with motor collimation was used for the LC experiments. A Plasma-Jet® PJ-08 electrospray deposition equipment was selected for the ESD depositions while a custom-made equipment was manufactured in order to produce the ENP coatings. Finally, EPSI® and MJ Engineering® laboratory units were employed for HIP processing.

In this paper, results obtained within tests in simulated geothermal conditions (Stage 3, Figure 1) are reported and therefore the only the setup employed in these tests will be described. Corrosion resistance properties were assessed by potentiodynamic polarisation resistance and Tafel scan measurements following the ASTM G102-89 standard. All potentiodynamic polarisation measurements were performed by using an ACM Instruments® Gill 16 electrochemical system while a Bank Elektronik GmbH® Azelle 5 avesta cell was employed for the Tafel scans. Electrochemical tests were performed in a 3.5% NaCl solution, 25°C and constant pH=4. These conditions, although not representative of the actual geothermal condition, has been employed uniquely for ranking purposes due to the significant number of specimens tested. Within Stage 4 in the project, the best performing specimens will be subjected to test in real geothermal environment. Custom-made equipment (SJS Engineering Ltd®), has been used for the erosion wear tests in this project, performed based on ASTM G76-13. For this test, 220 mesh white alumina was employed as grit, by setting a 90° impact angle between nozzle and substrate, for a total test duration of 140 s. The erosion-corrosion rate was established in a custom-made recirculating impinging slurry jet apparatus by using 400µm angular silica as erodent and a 90° nozzle to substrate relative angle. Contact angle measurements were performed by using a DSA 100 drop shape analysis system (Kruss GmbH®) by using de-ionized water as liquid medium.

Methodology

The rationale behind the use of the materials, deposition techniques, substrates and application to geothermal power plant components is depicted in Figure 1. It can be noted that the developed materials and deposition techniques are not intended for all components applications. It is also worth noting that HIP MMCs and Electroless plated duplex coatings are only intended for one component application, pump impellers and heat exchangers respectively. Conversely, deposition techniques ESD, LC and HVOF are intended for multiple components such as pipelines, casings, valves and turbines.

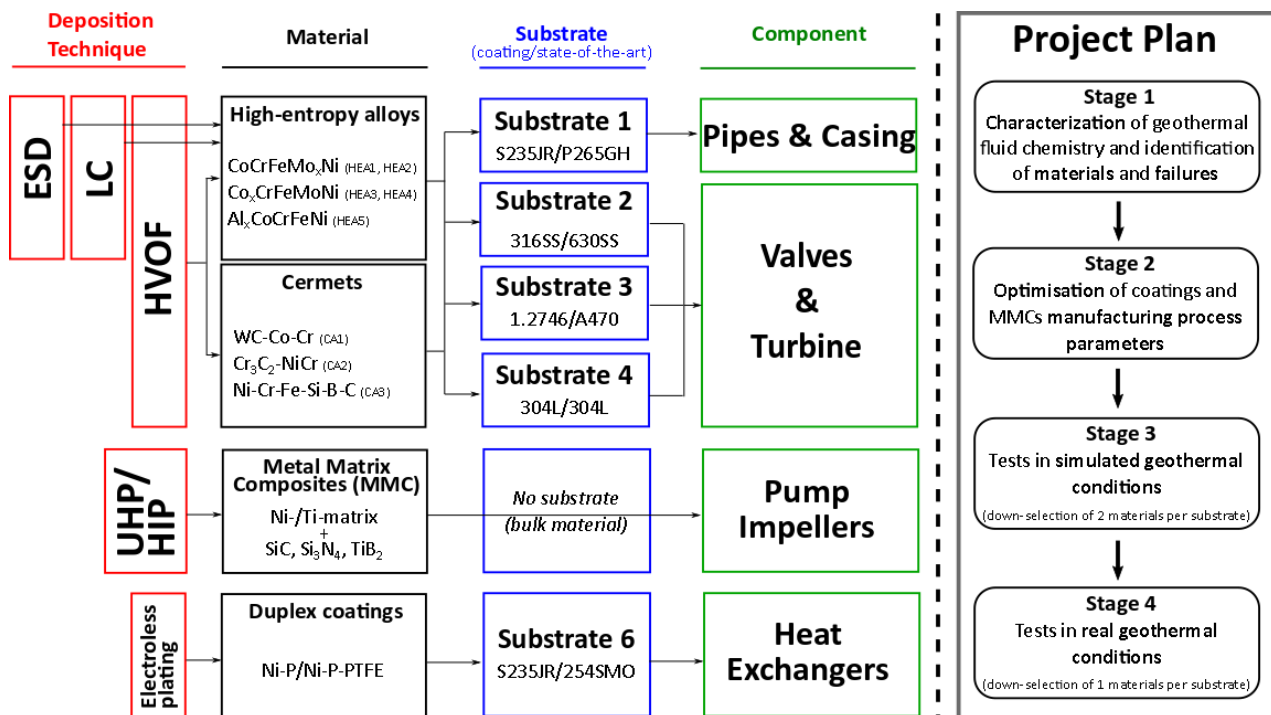


Figure 1 – Schematic view of deposition technique, materials, substrates and components targeted by the project together with a simplified project plan. The abbreviations refer to: ESD (Electrospark deposition), LC (Laser Cladding), HVOF (High Velocity Oxygen Fuel spray), UHP (Hot isostatic pressing)/HIP (Isostatic Hot Pressing). The substrates are subdivided into coating substrates and state-of-the-art substrates, where these latter have been tested without coating together with the coated substrates for comparison purposes. This paper presents preliminary results obtained up to Stage 3.

A simplified project plan is also reported on the right hand side of the figure. The project is subdivided into four main stages: (Stage 1), where characterization of the geothermal fluid within the Hellisheidi and Nesjavellir power plants is performed, together with a definition of the principal failure mechanisms within geothermal power plants, (Stage 2) where coating deposition and MMC manufacturing process parameters are optimized based on a microstructural analysis, (Stage 3) where the materials produced at the conditions optimized in Stage 2 are tested in simulated geothermal conditions, leading to a down-selection of two materials per substrate and (Stage 4), where the two materials per substrate selected within Stage 3 are further tested in real geothermal conditions, providing a final down-selection of one material per substrate. In the final phase of this latter stage, real components (e.g. pipes, heat exchangers, etc.) treated with the down-selected materials are also tested. The Flow Assurance Simulator (FAS, not reported in the figure) is developed in parallel to the other stages of the project, by taking inputs from the experimental analysis. In this paper, results obtained up to Stage 3 are reported.

3. PRELIMINARY RESULTS

3.1 Characterization of geothermal fluid chemistry and identification of materials and failures (Stage 1)

The initial phase of the project aimed to: (a) collect chemical data at several locations within the Hellisheiði and Nesjavellir power plants and (b) define the critical components of geothermal power plants, where the Geo-Coat technology could be employed. The chemical analysis have focused on specific components : production well fluids after the control valve, steam into turbines, gas from turbines, separator water after 1st flash, separator water after 2nd flash, separator water after heat exchangers, condensate, seal water, sulfix water and cooling water and typical groundwater. Temperature, pressure, pH, non-condensable gases (NCG) and amount of dissolved ions have been probed. A summary of the combined range values obtained from the two power plants is reported in Table 1. These values have been employed to specify the environment for the exposure tests in simulated geothermal conditions within the project.

Table 1 – Summary of combined chemical analysis from the different sampling locations at Hellisheiði and Nesjavellir power plants.

Location	State	T [°C]	P [bar]	pH	CO ₂ [mg/kg]	H ₂ S [mg/kg]	SiO ₂ [mg/kg]	Na [mg/kg]	K [mg/kg]	Ca [mg/kg]	Cl [mg/kg]	SO ₄ [mg/kg]	Se [mg/kg]
Wellhead	Water	176-209	16-77	7.12-8.67	4-29.1	7-105	204-1224	9.5-168.7	<4-36	0.32-0.46	5-205	1.5-13.4	0.82-46.9
	NCG	-	-	-	443-3807	410-1173	-	-	-	-	-	-	-
	Cond. steam	-	-	3.95-4.42	-	-	0.172-0.53	<0.1-0.13	<0.4	<0.1	0.08-1.8	0.3-1.6	<0.5-1.43
Steam into turbines	NCG	172-191	7.4-11.8	-	1268-3470	384-978	-	-	-	-	-	-	-
Gas from turbines	NCG	-	-	-	37-66 [vol%]	12-34 [vol%]	-	-	-	-	-	-	-
Separator water after 1st flash	Water	172-180	8.4-12	8.70-8.94	22-30	50-75	676-758	168-206	33-35	0.30-0.74	155-186	42705	n.a
Separator water after 2nd flash	Water	119	2-10	9.2	20	30	735	203	38	0.85	186	21.5	16
Separator water after heat exchangers	Water	10-85	10-12	8.83-9.2	19.8-23.7	30-82	735-764	159-206	31.6-35.5	0.27-0.78	118-186	18.1-24.4	7.6-15.3
Condensate	Water	40-60	1	5.1-6.9	2-20.9	1-98.3	<0.06-4.4	<0.1-1.78	<0.4	<0.1-0.86	<0.1-1	1-3.9	<0.5
Seal water	Water	40-60	1	n.a.	365-920	331-560	<0.06	<0.1	<0.4	<0.1	<0.1	7	0.535
Sulfix water	Water	15	7.5	n.a.	7100	4000	n.a.	n.a.	n.a.	n.a.	n.a.	n.a.	n.a.
Cooling water	Water	4	n.a.	7.3	25.7	0	24	6.3	0.9	4.56	5.8	1.4	<0.5
Typical ground-water	Water	-	-	7.72-8.3	-	-	24.1-34.9	6.2-14.8	0.88-1.67	4.8-9.5	7.0-13.2	2.2-10.5	<0.5

In order to identify the main sources of components failures, a comprehensive failure mode and effect analysis (FMEA) has been performed on results of a survey of 12 power plant operators geographically scattered worldwide. As a result, a list of the critical components, the principal damage mechanisms and the effect on the component operational behavior has been generated (see Table 2).

Table 2 – Critical components, principal damage mechanisms and their effects compiled from FMEA analysis from 12 different geothermal power plants.

System	Component	Part	Erosion	Corrosion	Scaling	Effect
Steam production	Wellhead	Casing below cellar		X		Material reduction – safety issue
		Ring tool joint	X	X		Leaking – safety issue
	Pipes	Liner			X	Reduced flow – reduced efficiency
		Casing			X	Reduced flow – reduced efficiency
	Valves	Seat	X		X	Can't seal – safety issue
		Stem	X			Can't seal – safety issue
	Pumps	Coil		X		Leaking – reduced efficiency
		Impeller	X		X	Damage - reduced efficiency
Steam transmission	Pipes	H ₂ S removal		X		Leaking – safety issue
		2 phase		X		Leaking – safety issue
		2 phase - inlet		X		Leaking – safety issue
		Steam pipe		X		Leaking – safety issue
	Valves	Pin	X			Can't seal – safety issue
		General			X	Sticking – safety issue
	Pumps	Shaft	X			Vibration – safety issue
		Bowl/barrel		X		Damage – reduced efficiency
	Steam cleaning/ separating	Separator vessel	X	X		Strength reduction – safety issue
		Steam scrubbing	X	X		Strength reduction – safety issue
		Stack		X		Leaking – safety issue
		Mist eliminator wire mesh		X		Breaking – reduced efficiency
	Turbine	Labyrinth seals	X		X	Stock up – reduced efficiency Leaking – reduced efficiency
		Diaphragm, outer edge	X	X		Bypass of fluid – reduced efficiency
		Diaphragm, inside outer ring	X	X		Blades can loosen – safety issue
		Nozzle blades			X	Clogging – reduced efficiency
		Rotor disc	X	X		Blades can loosen – safety issue
		Rotor drum	X	X		Reduces sealing – reduced efficiency
		Rotor blades	X	X		Damage – reduced efficiency
		Casing		X	X	Hinders flow – reduced efficiency Strength reduction – safety issue
			X			Bypass of fluid – reduced efficiency
	Heating/cooling	Pre-heater tubes		X	X	Clogging/leaking – reduced efficiency
		Pre-heater water caps		X		Leaking – safety issue
		Vaporizer tubes	X			Leaking – safety issue
		Condenser			X	Build-up – reduced efficiency
		Air cooling condenser tubes		X		Leaking – safety issue
		Air cooling condenser supports		X		Material reduction – safety issue
Reinjection	Pipes	Brine pipelines			X	System upset – reduced efficiency Leaking – safety issue
		Casing			X	Reduced capacity – reduced efficiency
				X		Leaking – safety issue
	Valves	Seat	X			Can't use to regulate – safety issue
		Brine check valve pin	X			Can't close – safety issue
		At wellhead - seat			X	Sticking – safety issue
		Pressure retention valve body		X		Not significant
		Check valve body		X		Not significant
		Check valve disc		X		Inoperable – safety issue
	Pumps	Impeller	X		X	Damage – reduced efficiency
Cooling	Pipes				X	Hinders flow – reduced efficiency

Results from this research have directed the focus of the study towards a few components: pipelines and casing, valves, turbine, pump impellers and heat exchangers (Figure 1).

3.2 Optimisation of coatings and MMCs manufacturing process parameters (Stage 2)

The corrosion-, erosion- and scaling-resistance performance of coatings and MMCs depends on both their physical-chemical properties (i.e. phases, grain size, etc.), and their microstructure (i.e. porosity, microcracks, etc.). Physical-chemical properties and microstructure are, in turn, defined by the production process parameters. The aim of this stage is therefore two-fold: (a) the down-selection of specific compositions and production method optimization for the initial powders and (b) the optimization of the production process parameters.

3.2.1 Down-selection of powders

While commercial powders and reagents were employed to produce MMCs and the duplex coatings, a combination of commercial and newly designed powder alloys have been selected for HVOF, LC and ESD coating manufacturing. For these deposition techniques, both cermets (commercial, for HVOF deposition only) and high-entropy alloys (HEA, custom-made, for HVOF, LC and ESD deposition) have been selected (Figure 1).

For the HEA, compositions were selected from first principles calculations on thermodynamic properties of the alloy material, aiming at final alloys composed of (a) solid solutions and (b) a mixed FCC-BCC crystal structure. It is expected, in fact, that an alloy composed of a homogeneous solid solution would possess better corrosion resistance properties compared to a system with mixed phases, due to potential galvanic effects in this latter case. Moreover, depending on the specific operational environment, a combination of the more ductile FCC structure with the tougher BCC is expected to provide ideal mechanical properties. For HEA systems, it is found that the final crystal structure is determined by specific thermodynamic parameters [16, 17]: valence electron concentration (VEC), mixing entropy (ΔS_{mix}), mixing enthalpy (ΔH_{mix}) and atomic size difference (δ). In this work, alloys of the compositions $\text{CoCrFeMo}_x\text{Ni}$, $\text{Co}_x\text{CrFeMoNi}$ and $\text{Al}_x\text{CoCrFeNi}$, were produced, where the index x was determined by selecting alloys falling within given limits of thermodynamic parameters: $\text{VEC} \sim 7.8$, $11 \leq \Delta S_{\text{mix}} \leq 19.5$, $-22 \leq \Delta H_{\text{mix}} \leq 7$, and $0 \leq \delta \leq 8.5$ in an attempt to meet the aforementioned conditions of solid solution and mixed FCC-BCC crystal structure. In this way, five specific HEA compositions have been selected. Moreover, since it is expected that the powder manufacturing process will affect the microstructure of the deposited coatings, one of the selected HEA compositions was manufactured by means of two manufacturing methods: mechanical alloying (MA) and gas atomization (GA). SEM micrographs of the as-produced powders are reported in Figure 2. Powders and reagents employed for MMC and ENP coatings productions are not reported.

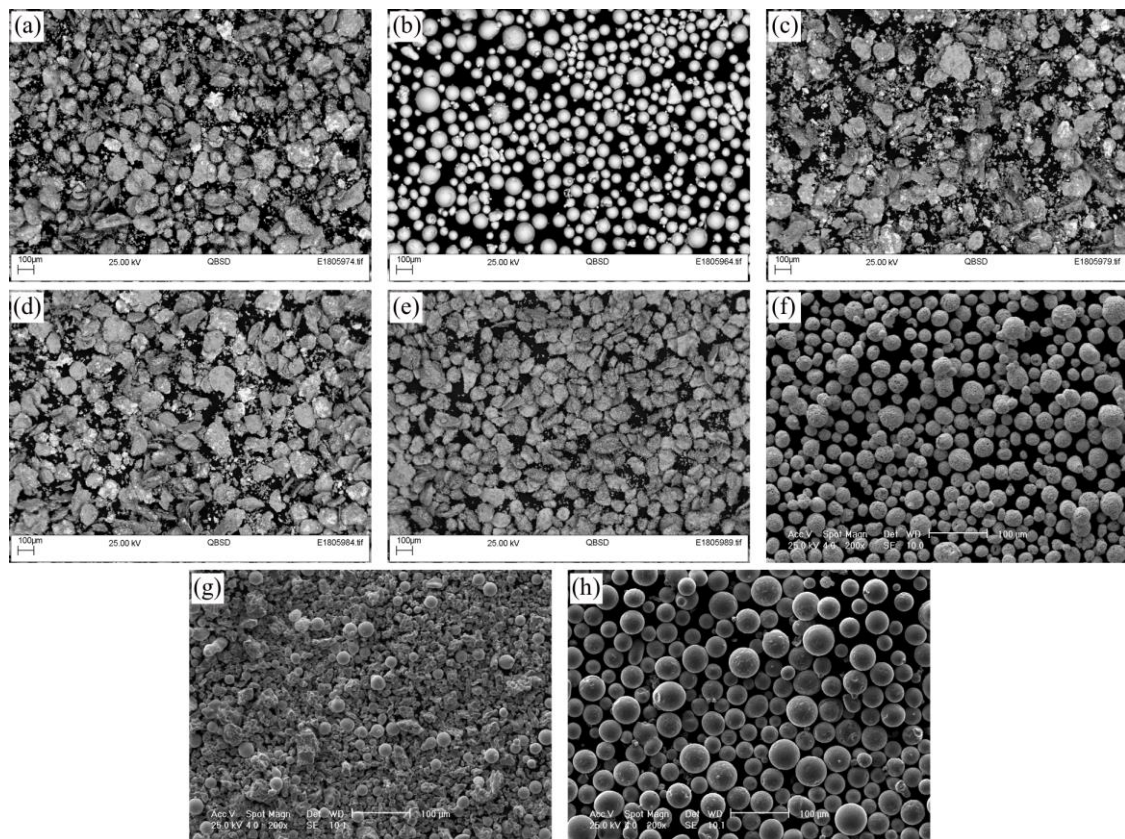


Figure 2 – SEM micrographs of the HEA and cermet powders used to produce the HVOF, LC and ESD coatings in the work:
 (a) HEA1 – mechanically alloyed $\text{CoCrFeMo}_x\text{Ni}$, (b) HEA2 – gas atomised $\text{CoCrFeMo}_x\text{Ni}$ of the same composition as (a) (c) HEA3 – mechanically alloyed CoCrFeMoNi (d) HEA4 – mechanically alloyed $\text{Co}_x\text{CrFeMoNi}$ (e) HEA5 – mechanically alloyed $\text{Al}_x\text{CoCrFeNi}$ (f) CA1 – WC-Co-Cr cermet, (g) $\text{Cr}_3\text{C}_2\text{-NiCr}$ cermet and (h) CA3 – Ni-Cr-Fe-Si-B-C cermet.

The batches of powders so-obtained were sieved and several size distributions were prepared for different deposition techniques.

3.2.2 Process parameters optimization

In this stage, an experimental design was executed, aimed at producing coatings with minimal amount of defects, e.g. porosity, cracks and unwanted phases. To this aim, specific deposition process parameters were varied and the effect of their variation onto the coating microstructure was assessed for each deposition/production technique. As an example, optical micrographs of the cross-sections of laser cladding depositions by using the HEA2 powder onto a carbon steel substrate (Substrate 1 - S235JR) are reported in Figure 3, which depicts laser clad single tracks with different outcomes in terms of coating microstructure. Figure 3(a) shows a clad where significant dilution, likely due to excessive laser power, has occurred with additional presence of spherical porosity generated at the root of the clad area. The opposite effect is observed in Figure 3(b) where, due to insufficient laser power, no deposition could be attained. Finally, reduced dilution and minimized presence of porosity is observed in the specimens of Figure 3(c), where adequate process parameters have then been employed for the powder under analysis.

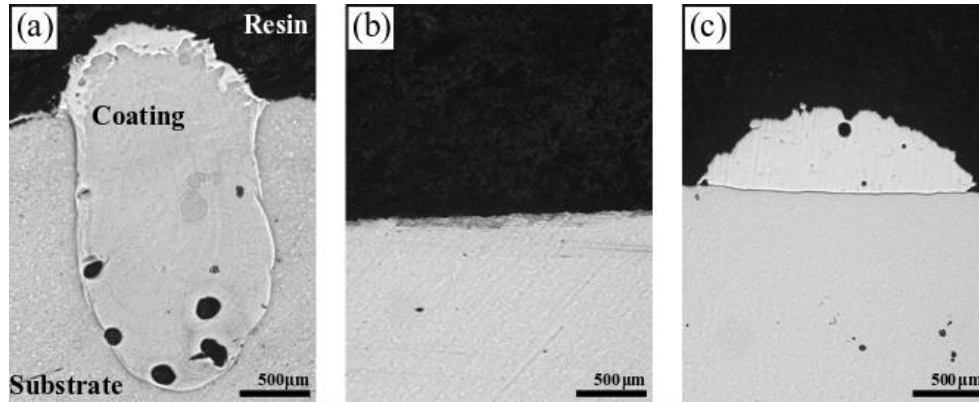


Figure 3 - Optical micrographs (cross-section) of some of the LC trial coatings produced from the HEA2 powder onto substrate 1 – S235JR, in the process parameters optimization phase, showing (a) excessive dilution and porosity, (b) no deposition and (c) minimized dilution and reduced porosity. The process parameters conditions employed for specimen (c) have been selected for further deposition.

Some of the optimized microstructures obtained from each of the deposition/production techniques employed in the project are reported in Figure 4.

Figure 4(a) shows the microstructure of a HVOF coating produced from the mechanically alloyed powders HEA1. Separate phases can be observed within the coating, denoted by a different coloration, together with a degree of porosity, showing as darker areas. EDX and XRD analysis showed that the lighter phases in the coating are consistent with a Mo-rich BCC crystal structure, while the grey areas are linked to a FCC structure, characteristic of Ni, Fe and Cr elements. This phase separation is given by the HEA1 powder manufacturing process, mechanical alloying which, at the manufacturing parameters employed in this work, provides particles of non-homogeneous composition (Figure 2). Conversely, it is worth noting that a more homogeneous microstructure (not shown) is observed in HVOF – HEA2 coatings, due to the homogeneous microstructure within the as-manufactured powder. A denser microstructure is obtained in the LC – HEA2 specimens (Figure 4(b)), due to the fact that, compared to the HVOF process, a high energy density, slower cooling rates and the presence of convective motion within the molten pool are provided by the LC process. Homogeneity is also characteristic of the ESD – HEA4 coating (Figure 4(c)), although the presence of micron and sub-micron sized porosity is observed and a significantly lower overall thickness compared to HVOF and LC coatings. The microstructure of the MMC specimen, HIP – Ti6Al4V+10wt.%TiB₂, is shown in Figure 4(d). It is worth noting how the processing at elevated temperature and pressure has resulted in a consolidated Ti-6Al-4V matrix composed of α (red) and β (white) phases with inclusions of TiB phase (black), which has transformed from the original TiB₂ stoichiometry by interaction with the Ti present in the matrix. It is expected that the presence of these inclusions would improve the mechanical properties of the material compared to a pure Ti-6Al-4V matrix for a pump impeller application. Finally, the microstructure of the topcoat layer of a duplex Ni-P/Ni-P-PTFE ENP coating (i.e. the Ni-P-PTFE) is shown in Figure 4(e). The dispersed PTFE particles are present as dark phases of hexagonal shape. It is expected that these particles would reduce the coating surface energy compared to a standard Ni-P composition, which could benefit the scaling resistance properties for heat exchangers applications.

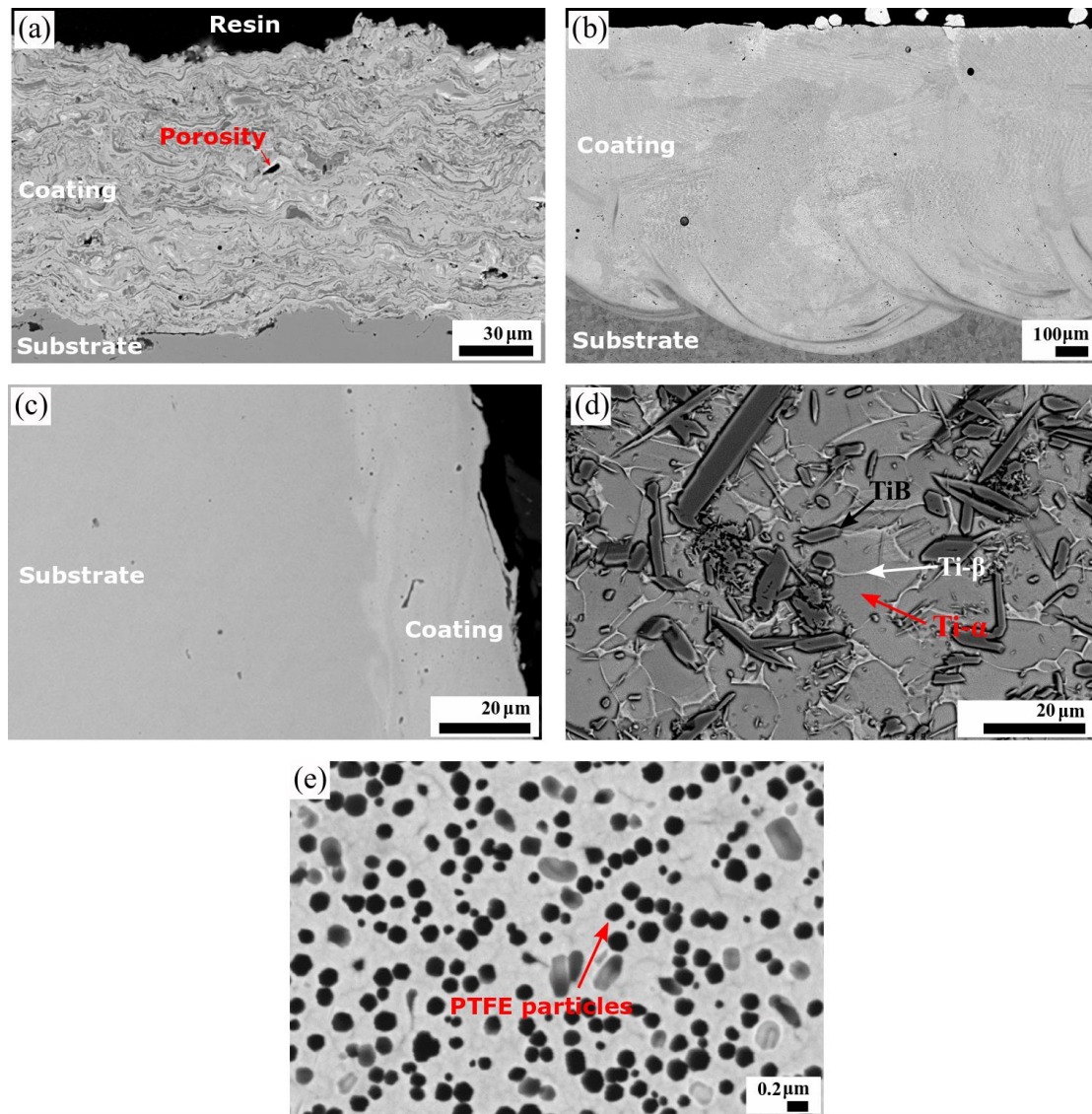


Figure 4 – SEM micrographs of some of the coatings and MMCs produced in the work: (a) HVOF - HEA1, (b) LC – HEA2, (c) ESD – HEA4, (d) HIP – Ti6Al4V + 10wt.%TiB₂ (e) ENP – Ni-P-PTFE layer.

3.3 Tests in simulated geothermal conditions (Stage3)

Coatings and MMCs manufactured with the optimized process parameters on all the required substrates (see Figure 1), have been first tested in simulated geothermal conditions in order to assess their corrosion, erosion wear and erosion-corrosion wear resistance properties. Two coatings/MMCs per substrate, as down-selected from this stage, are currently being tested in real geothermal conditions.

3.3.1 Corrosion resistance

Corrosion, whether uniform or in form of pitting, crevicing, etc. or combined with erosion-type damage, is a common cause of failure for components of geothermal power plants (e.g. well casing pipes and transportation pipes). LPR testing, coupled with Tafel scan, was employed in this stage. Although minimized during the optimization of the production process parameters, the coatings and MMCs produced can contain defects, such as cracks, porosity, etc. It is expected that the presence of these defects, if present, could make the system permeable to the corrosive solution, with consequent exposure of the substrate. As an example, Figure 5 shows the exposed surface of two LC specimens deposited on the four substrates S1-S4, HEA1 (a-d) and HEA3 (e-h), all produced from mechanically alloyed powders.

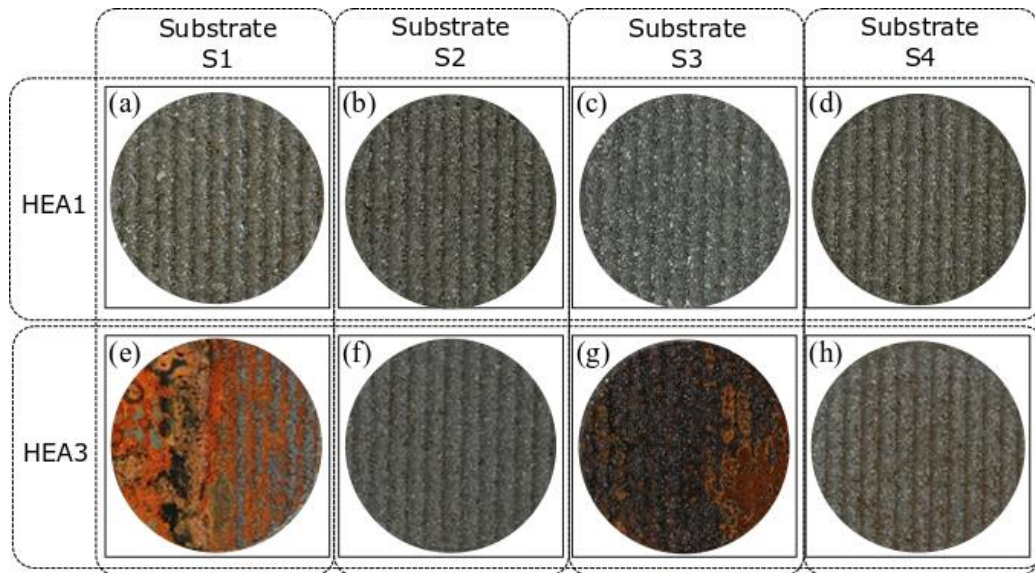


Figure 5 – Photograph of exposed surface for LC coatings obtained from mechanically alloyed powders HEA1 (a-d) and HEA3 (e-h). Results are reported for the coatings deposited onto substrates S1 (a and e), S2 (b and f), S3 (c and g) and S4 (d and h), demonstrating how solution permeation through the coating has occurred for the HEA3 system. For details on substrates see Figure 1.

The four substrates employed are carbon steel (S1, S3) and stainless steel (S2, S4). All of the uncoated areas of the specimens, including the substrate, have been protected by a polymeric lacquer inert to the corrosion solution, and it is therefore expected that only the coating surface would be exposed to the corrosive medium. Therefore, if the coatings act as a barrier to the corrosive medium, it is expected that dissolution of the coating, and not substrate, would be observed. Figure 5 seems to show two systems, LC-HEA1 (a-d) and LC-HEA3 (e-h) with different behavior. In the former case, the surface appearance seems visually comparable irrespective of the substrate employed. In the latter instead, corrosion products seem to be only prevalent on the surface of coatings deposited on substrates S1 and S3 (carbon steels), while only a light discoloration is shown by the coatings deposited on stainless steels S2 and S4. This behavior could suggest that permeation is occurring through the LC-HEA3 coating, leading to the preferential (and rapid) corrosion of the carbon steel substrates in the case of substrates S1 and S3.

The corrosion rate, calculated for each coating as an average over the values measured on the system on all substrates S1-S4 are presented in Figure 6 together with wrought alloys for comparison. Results for the MMC materials are not reported in the figure, due to the fact that this class of material was only tested in erosion-corrosion (see Paragraph 3.3.3). It is worth noting that values of calculated corrosion rate are only reported for some of the tested systems and are reported as full black bars. Conversely, the values of the specimens with the empty bars correspond to coated systems where permeation has been observed, and to which therefore a coating corrosion rate could not be assigned.

An analysis of the results obtained should be performed according to the testing plan (Figure 1). The lowest measured corrosion rate is shown by the electroless plated coating ENP-Ni-P/Ni-P-PTFE system, intended for heat exchanger applications. Its value should therefore be compared to the one of substrate S6-254SMO, which shows a comparable level (0.0018 for this latter vs 0.0019 mm/y for the coating). The lowest value for the coated systems intended for applications on substrate S1 to S4 (i.e. pipes & casing and valves & turbine) has been measured in system LC-HEA2, which shows a value, 0.0022 mm/y, lower than any rate measured on the standard wrought alloys measured for the four substrates. It is worth noting that the result for specimen HVOF-HEA5 is missing since no significant deposition could be achieved by using this powder material. Moreover, none of the electrospray (ESD) deposited coating proved effective as a corrosion barrier during the tests, likely due to the presence of defects in these systems.

3.3.2 Erosion wear resistance

Although generally not encountered as single cause of failure in geothermal power plant components, erosion wear, often combined with the corrosion-type of damage can be generated by dispersed particles or at regions of local flashing of the geothermal fluid. The coatings resistance to air-entrained solid particle impingement erosion has been performed by using white alumina as grit medium for the coated specimens corresponding to pipes, casings, valves and turbine applications (i.e. substrates S1 to S4 in Figure 1). The results, in terms of total weight loss after the test, are presented in Figure 7.

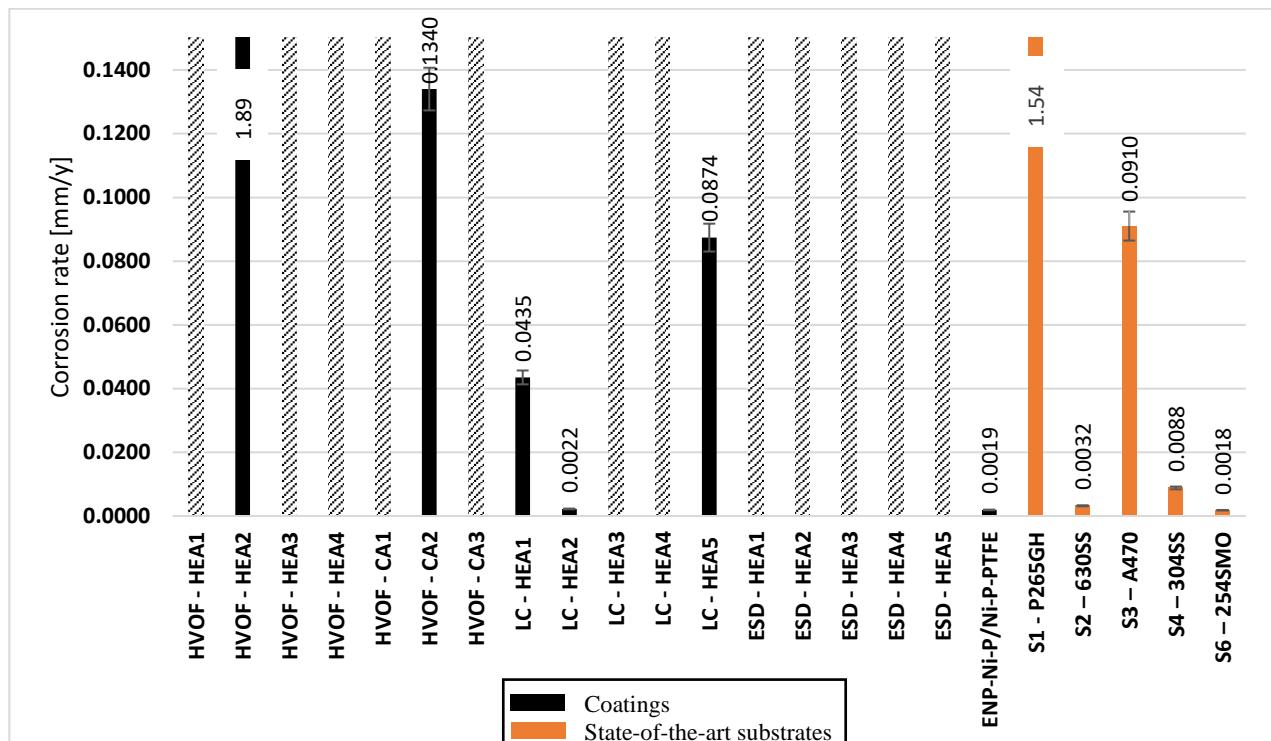


Figure 6 – Corrosion rate results (mm/y) at the end of the exposure time, calculated for each manufactured coating as an average over the values measured on all four substrates S1-S4, together with additional standard wrought alloys for comparison. The system LC-HEA2 performed better than any of the comparison wrought alloys tested for substrates S1 to S4, and coating ENP Ni-P/Ni-P-PTFE shows comparable results against the S6-254SMO wrought alloy. Notice that the values in grey correspond to systems where permeation has been observed, for which a value for the corrosion rate of the coating could not be reliably calculated. For details on substrates see Figure 1.

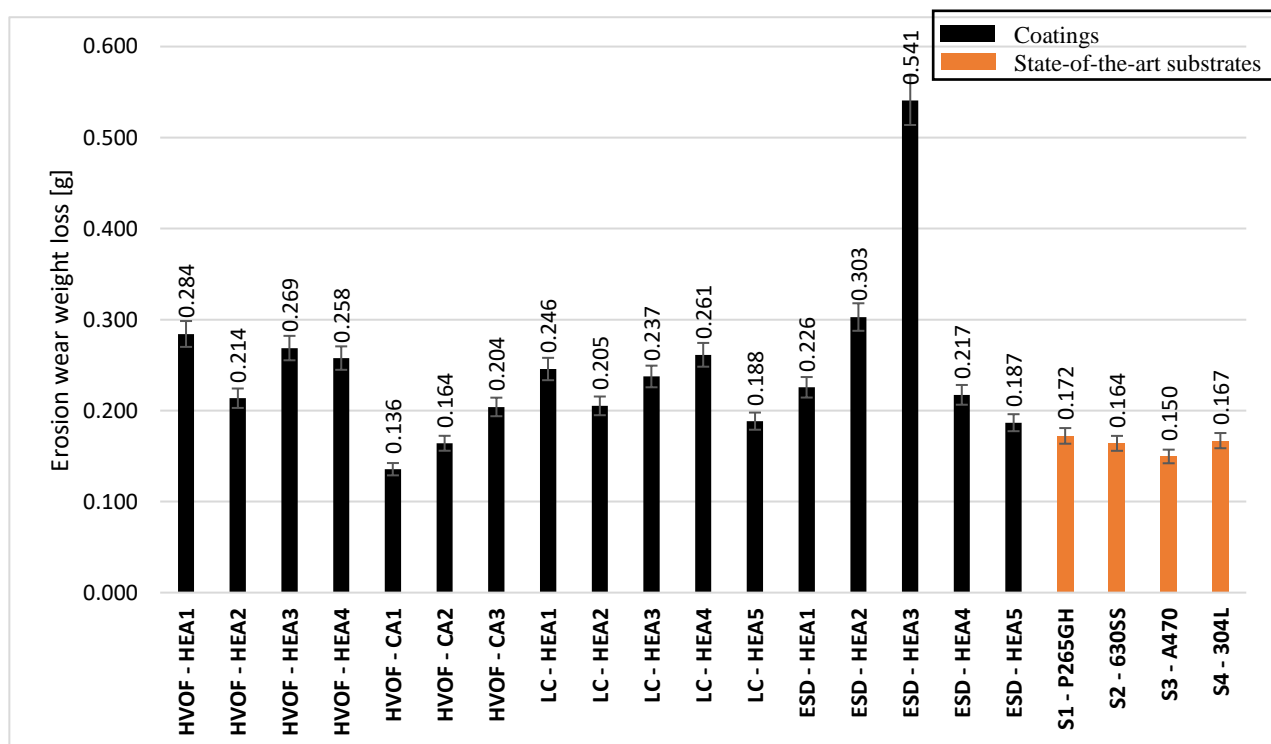


Figure 7 – Erosion wear weight loss, measured as total mass lost after the test. All of the specimens for this test have been deposited onto substrate S1 only. Among the tested coatings, the cermet HVOF powders CA1 and CA2 performed well, even compared to the standard wrought alloys substrates. For details on substrates see Figure 1.

It is worth noting that, amongst all the tested specimens, the HVOF-deposited cermet powders CA1 and CA2 perform well, even if compared to the wrought alloys. High values are generally shown by the ESD coatings, possibly due to their brittle nature and presence of defects, which could also explain their low corrosion resistance performance (Figure 6). It is expected that the resistance

of a material to solid particle impact is related to its toughness and thus denser materials would tend to perform better in such an environment. In this respect, HVOF coatings (Figure 3(a)), produced by the overlap of single splats of molten material, would be expected to perform worse when compared to denser LC systems (Figure 3(b)) or wrought alloys. This has been proven by comparing the same HEA powders deposited by HVOF and LC, with these latter providing better results than the former. Moreover, the remarkable results obtained by the HVOF cermet powders compared to any of the other tested systems are very promising.

3.3.3 Erosion-corrosion wear resistance (MMCs for pump impellers)

The combined effect of corrosion and erosion is the main damage mechanism experienced by geothermal pump impellers. For this reason, the MMCs produced in this work were tested under erosion-corrosion load. The results from the tested systems, including the state-of-the-art substrates S5-IN625 and S5-Ti64 are reported in Figure 9.

The results highlighted in red correspond to specimens only tested in erosion wear (no corrosion) due to their excessive porosity, which hinder the possibility of measuring a reliable weight loss under erosion-corrosion conditions. It is worth noting that the values measured for the UHP-manufactured MMCs result generally higher than the values measured for the HIP systems. From microstructural analysis, this has been linked to the significant porosity of the UHP compared to HIP MMCs. It is likely that the UHP conditions employed were generally not sufficient to obtain a homogeneous microstructure. As an example, the SEM micrograph of the UHP-Ti6Al4V+10wt.%TiB₂, corresponding to the HIP system of the same composition in Figure 4(d), is reported in Figure 8.

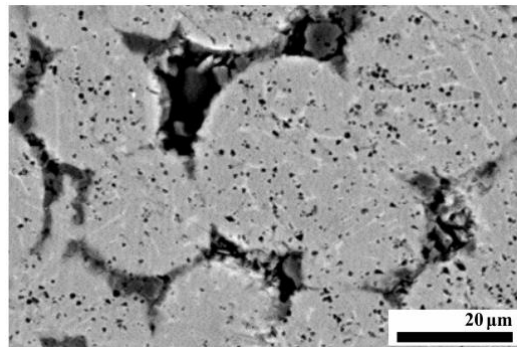


Figure 8 – SEM micrograph of MMC specimen UHP-Ti6Al4V+10wt.%TiB₂ showing presence of porosity and a less homogeneous microstructure compared to the HIP specimen of the same composition (Figure 4(d)).

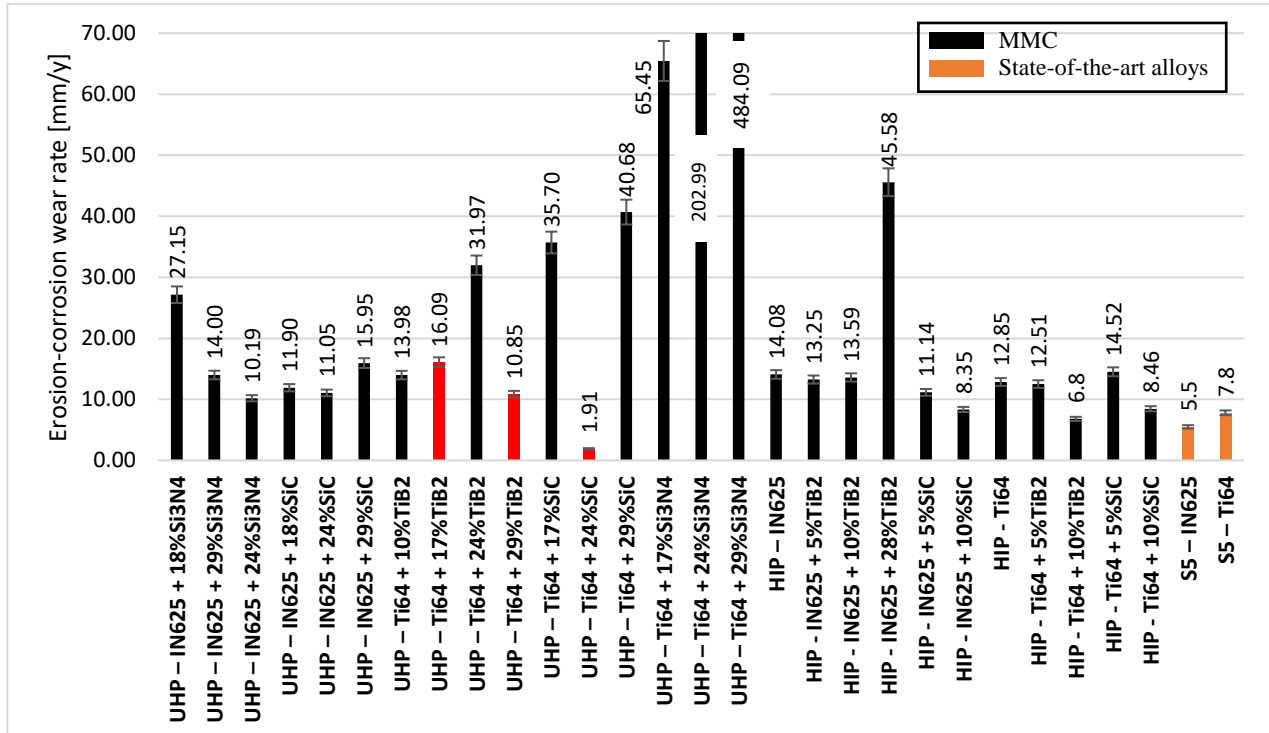


Figure 9 – Erosion-corrosion wear rate measured on the MMC materials. The UHP-manufactured MMCs showed higher wear rate due to significant porosity. Specimens highlighted in red have been tested only in erosion wear as a reliable weight loss in erosion-corrosion conditions could not be obtained due to excessive porosity. For details on substrates see Figure 1.

Among the tested specimens, HIP-IN625+10wt.%SiC and HIP-Ti64+10wt.%TiB₂ exhibited the lowest wear rate, in the latter case, even lower than the value for the corresponding state-of-the-art wrought alloy substrate S5-Ti64.

3.3.4 Cost and overall ranking per substrate

Based on the results of the tests and by adding further cost comparison, an overall ranking was performed for each substrate/application in Figure 1. Based on the ranking, two systems (coatings/MMCs) per substrate type have been selected for further analysis in Stage 4 of the project. All the coatings/MMCs deposited on each substrate were assigned a score between 0 (worst) and 10 (best), with contributions provided by corrosion (from corrosion rate), tribological (from erosion wear, erosion-corrosion wear and scaling) and cost performance. For each substrate, each performance property has been given a weightage value (0-100%), based on the likelihood of the damage mechanism to be relevant for the specific application (for tribological and corrosion performance) or on the value of the application (e.g. cost saving is more relevant for pipelines due to their extended area, while it is less important for pump impellers due to their high value). The cost was calculated as cost of 1 μm thick coating over a 1 m^2 substrate area (for HVOF, LC and ESD coatings), per $9.04 \cdot 10^{-4}$ and $2 \cdot 10^{-5} \text{ m}^3$ (for HIP and UHP MMCs respectively, given by the volume of the billets obtained in this work) and per 25 and 5 μm thick coating over a 1 m^2 substrate area (ENP topcoat and undercoat respectively). The selected systems, for each substrate/application, are summarized in Table 3.

Table 3 – Summary of coatings and MMCs selected for further testing (Stage 4) based on overall ranking on corrosion, tribological and cost performance.

Substrate	Substrate application	1 st system selected	2 nd system selected
S1	Pipes & Casing	HVOF – CA2	LC – HEA2
S2	Valves & Turbine	HVOF – CA2	LC – HEA2
S3		HVOF – CA2	LC – HEA2
S4		HVOF – CA2	LC – HEA5
S5	Pump impellers	HIP - IN625 + 10%SiC	HIP – Ti64 + 10%TiB ₂
S6	Heat exchangers	<u>undercoat</u> high P content, <u>topcoat</u> High P content, medium PTFE, no heat treatment	<u>undercoat</u> high P content <u>topcoat</u> Low P content, medium PTFE, no heat treatment

For the sake of comparison, the overall ranking score for the systems in Table 3, subdivided into corrosion, tribological and cost performance contributions is reported in Figure 10. It is interesting to note that a higher ranking score (i.e. overall better performance) is generally exhibited for the systems designed within the project compared against the state-of-the-art wrought alloy substrates. The only exceptions are the rankings for substrate S4 (Figure 10(d)) and S5 (i.e. MMCs, Figure 10(e)). In the former case, the same material, i.e. 304 stainless steel, has been employed both as coatings substrate and comparison wrought alloy. Since any coating operation only adds additional cost to the single substrate material, the cost of a coated component of comparable corrosion and tribological performance (which is what observed in this case) would always be higher than the same un-coated substrate material. It is worth noting, however, that values of other performance indicators for the same substrate can be higher than the comparison alloy, as in the case of tribological performance of HVOF-CA2 versus S4-304SS (Figure 10(d)). The cost also seems to play a predominant role in the ranking of the MMC materials (Figure 10(e)), although the tribological performance of HIP-Ti64+10wt.%TiB₂ has been observed exceeding the value of its corresponding wrought alloy S5-Ti64. Therefore, for the cases described above, it is possible for the overall lifetime of the new (coated/MMC) system to considerably exceed the lifetime of the state-of-the-art wrought alloy, therefore making the use of the new system advantageous.

It is worth specifying, however, that the ranking performed is based on results of tests in simulated geothermal conditions and are thus not fully representative of the actual conditions experienced in service. More insights will be provided by tests in real geothermal conditions on the two systems per substrate/application selected. This part of the work will be performed within Stage 4 in the project (Figure 1).

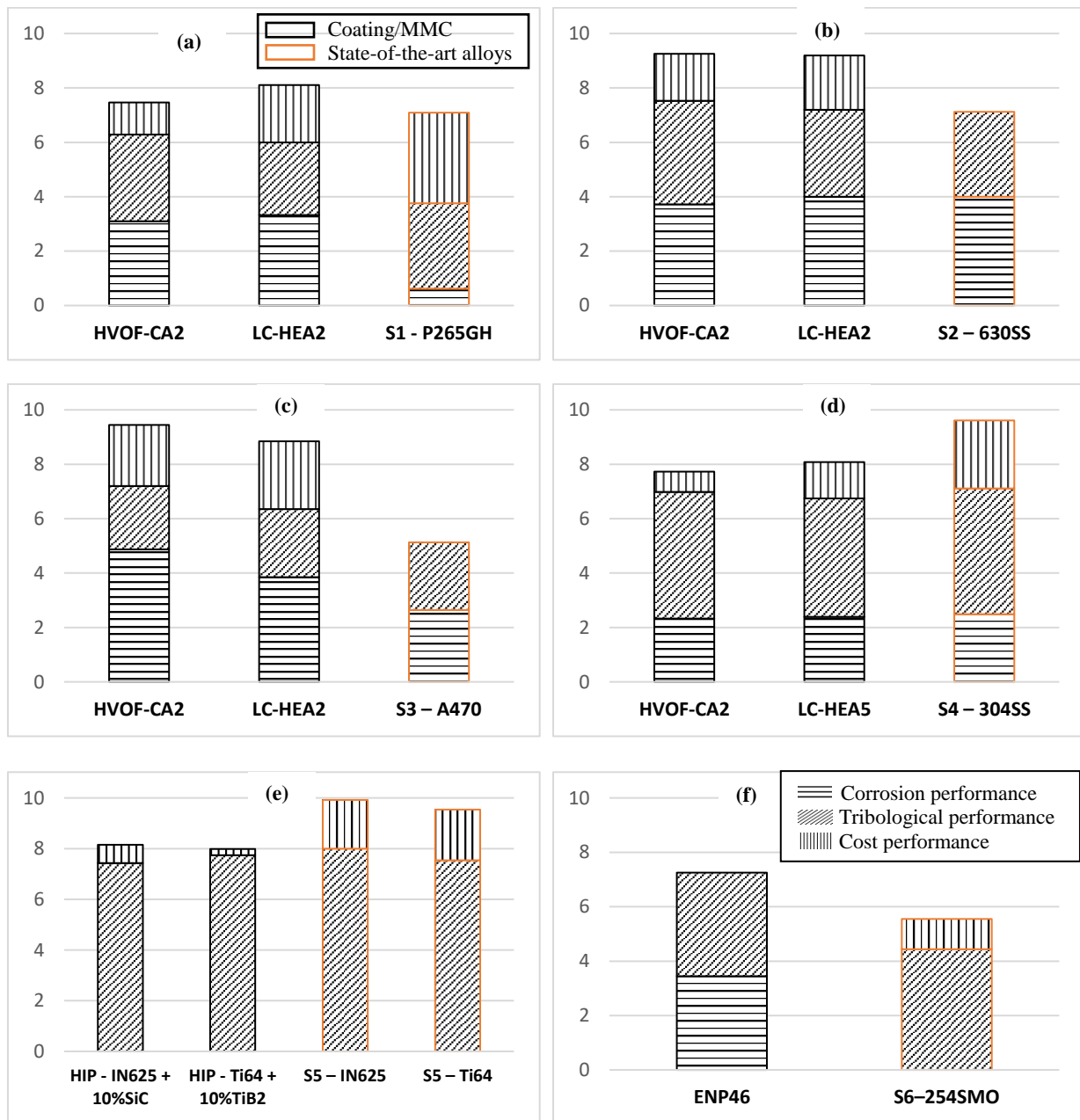


Figure 10 – Breakdown of ranking score (0-10) for the systems selected for each substrate/application (a) S1, (b) S2, (c) S3, (d) S4, (e) S5, (f) S6 including contributions from corrosion (horizontal lines), tribological (diagonal lines) and cost performance (vertical lines). The newly created materials outperform the state-of-the-art wrought alloys (highlighted in orange) in most cases, with exceptions given by systems on substrates S4 and S4 (MMCs) due to cost considerations. However, even in these cases, values of corrosion and tribological performance can be found to exceed the same quantities in the wrought alloys, therefore making the systems nevertheless promising.

3.4 Development of geothermal Flow Assurance Simulator (FAS)

In order to optimize geothermal coatings in a geothermal powerplant, it is important to have a good understanding of the operating conditions (e.g. temperature, pressure, flow rates) and geothermal fluid properties (e.g. composition, reaction rates, gas/liquid phase fractions, density, viscosity, heat capacity, heat conductivity, etc.) in the different parts of the piping system. For this purpose, FlowPhys1D, a new pipe flow network solver is under development in the GeoCoat project. To properly simulate the complex governing phenomenon involved, the simulator needs to combine thermodynamics, fluid dynamics, and geochemistry. This kind of modelling is called flow assurance and originates from the oil and gas industry, especially for offshore fields where multiphase flow need to be operated within the correct parameters to avoid or limit solid deposits such as hydrates, scale, wax, and unwanted flow regimes such as excessive slugging, and operational procedures such as start-up, shut in, injection of inhibitors, etc. The term flow assurance was first used by Petrobras (Garantia do Escoamento), meaning literally “guarantee of flow”. Flow assurance modelling is a relatively new area and is rapidly becoming widely used in the oil & gas industry where it is considered to be one of the most important key technologies for efficient, economical and safe oil & gas production.

The FlowPhys1D dynamic two-phase pipe flow network solver is based on a finite element approach, in which the mass and momentum equations are solved coupled while the energy equation is solved sequentially. The solver takes into account mass, heat

flux, pressure, and temperature for the pipe network joints. The two-phase flow is modelled with either a homogeneous flow model or a drift-flux model. Heat transfer between the fluid inside the pipe, pipe wall, insulation layer, and ambient environment is also included in the formulation. The software is of general character and can in principle analyze any pipe network. The erosion/corrosion/scaling models are under development and not shown in this paper. For both the homogeneous and the drift-flux two-phase flow models, the flow, mixture density, viscosity, heat capacity, and thermal conductivity are calculated as:

$$\bar{\rho} = \alpha_g \rho_g + \alpha_l \rho_l \quad (1)$$

$$\bar{\mu} = x \mu_g + (1 - x) \mu_l, \quad (2)$$

$$\bar{C} = x C_g + (1 - x) C_l \quad (3)$$

$$\bar{k} = x k_g + (1 - x) k_l \quad (1)$$

The heat transfer to ambient environment is calculated from:

$$q_r = \frac{T_{Fluid} - T_{Ambient}}{\frac{1}{2\pi r_1 L h_1} + \frac{\ln \frac{r_2}{r_1}}{2k_A \pi L} + \frac{\ln \frac{r_3}{r_2}}{2k_B \pi L} + \frac{1}{2\pi r_3 L h_3}} \quad (5)$$

where the heat transfer coefficients between the fluid and the inner pipe wall, h_1 , and the heat transfer coefficient between the outer insulation layer and the surrounding environment are calculated from:

$$h_1 = \frac{Nu * k_F}{D_1} \quad (6)$$

$$h_3 = 8 + 0.04(T_{Ambient} - T_3) \quad (7)$$

The Nusselt number is calculated from the Gnielinski correlation:

$$Nu = \frac{\left(\frac{f}{8}\right)(Re - 1000)Pr}{1 + 12.7(Pr^{\frac{2}{3}} - 1)\sqrt{f/8}} \quad (8)$$

Using the mixture Reynold's number, \overline{Re} , the Darcy-Weisbach friction factor is calculated from Haaland's approximation of the Colebrook-White equation:

$$f = f_L = \frac{64}{\overline{Re}} \quad \overline{Re} < 2000 \text{ (laminar flow)} \quad (9)$$

$$f = f_t = \left\{ -1.8 \log_{10} \left[\frac{6.9}{\overline{Re}} + \left(\frac{\varepsilon}{3.7D} \right)^{1.11} \right] \right\}^{-2}, \quad \overline{Re} > 4000 \text{ (fully turbulent flow)} \quad (10)$$

$$f = y f_t + (1 - y) f_L, \quad y = \frac{\overline{Re}}{2000} - 1, \quad 2000 < \overline{Re} < 4000 \text{ (transitional flow)} \quad (11)$$

The homogeneous two-phase model assumes that both phases have the same velocity, an assumption that is accurate in for example bubbly flows. However, for cases where the liquid and gas phases have different speeds, such as for example stratified or annular flows, a more accurate model, the drift flux model, has been implemented. This model uses a slip velocity model:

$$v_g = C_o \bar{v} + v_d \quad (2)$$

where:

$$C_o = \frac{2.27}{1 + \left(\frac{\overline{Re}}{1000}\right)^2} + \frac{1.2}{1 + \left(\frac{1000}{\overline{Re}}\right)^2}, \quad \text{and} \quad v_d = 0 \quad (3)$$

Results from a simplified pipe network test case are shown in Figure 11. The model geometry consists of a main pipe ("Pipe 1") and a small pipe loop ("Pipe 2"). The temperature distribution of the fluid inside the pipe after it has reach equilibrium is shown in Figure 11 (a). The temperature time history at the middle of the top pipe (Pipe 2) is shown in Figure 11 (b), while temperature profiles in Pipe 2 are shown in Figure 11 (c) and (d). The ambient air was set to 5 C; the pipe diameter 0.5 m, and the pipe insulation 20 cm of Rockwool. The fluid flow inside the pipe was flowing with a low speed to exaggerate the temperature gradients for easier visualization due to higher heat losses to the environment. The fluid inside the pipe was water in both gas and liquid form, with a liquid holdup (HL) varying from HL=0 % (pure gas) to HL=100% (pure liquid). From Figure 11 (b), for which the pipes were uninsulated, it is seen that it takes about 2000 s for the temperature to settle and also that cases with less liquid holdup have lower temperatures due to less energy content because of lower density and heat capacity, leading to a proportionally larger share of its heat energy lost through the pipe walls to the surroundings. This is seen even clearer in Figure 11 (c), where Pipe 2 profiles of different liquid holdup scenarios are plotted. In Figure 11 (d), 20 cm of Rockwool insulation has been added to the outside of the pipes, which results in much less energy lost to environment.

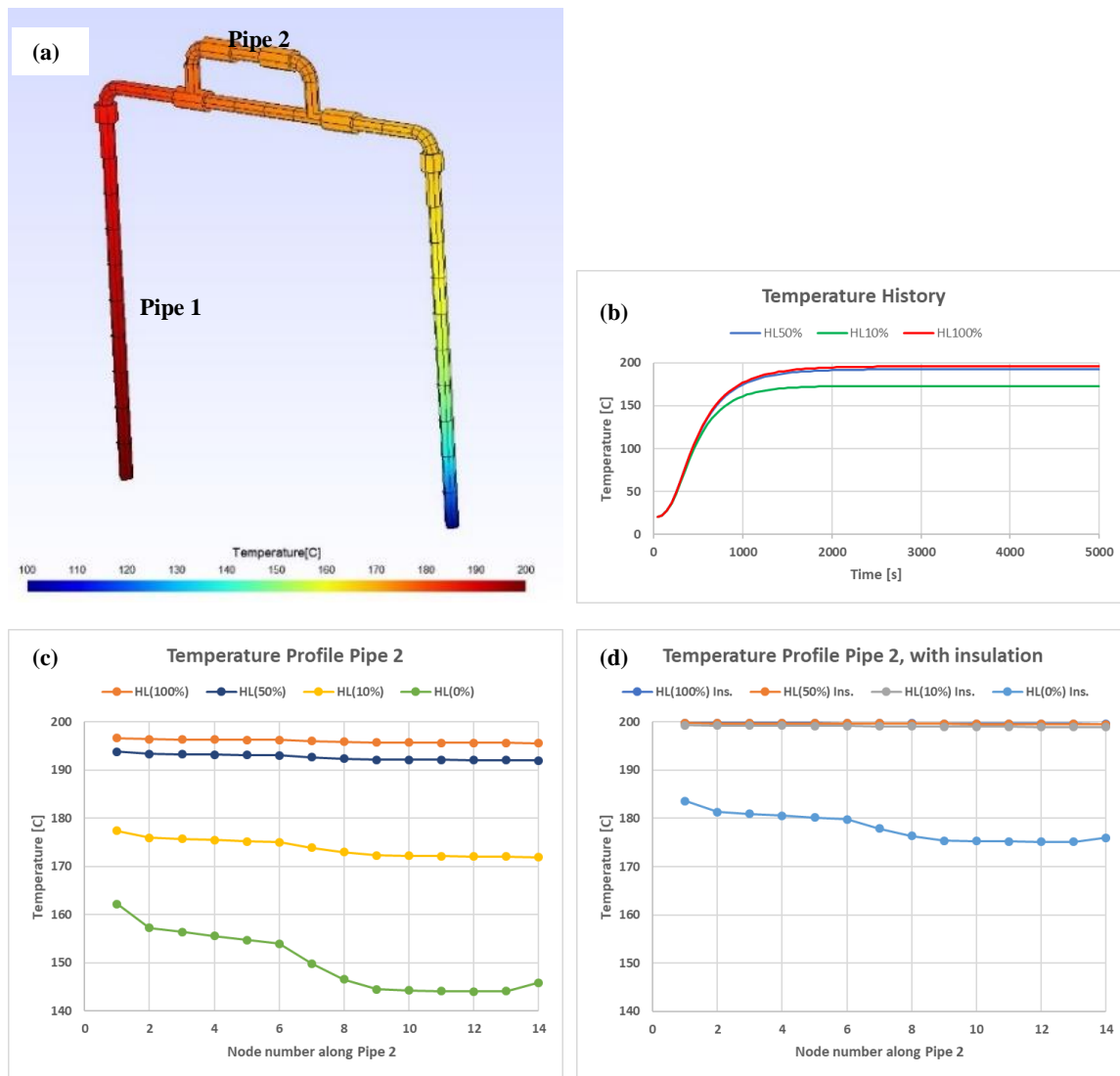


Figure 11 – Simulations of two-phase flow in a pipe network: (a) fluid temperature with two-phase flow of steam + water with 10% liquid holdup, (b) fluid temperature time-history at middle of loop 2 for different liquid holdups; (c) Pipe 2 temperature profiles with different liquid hold ups; (d) same as in (c) but with 20 cm of Rockwool insulation.

4. CONCLUSIONS

In order to decrease operational and capital expenditure in geothermal power plants, novel corrosion and erosion resistant coatings have been developed, tested and compared to state-of-the-art wrought alloys. At the same time, a Flow Assurance Simulator (FAS) has been developed, which is able to simulate and predict the location and extent of erosion, corrosion and scaling damage by modelling the thermodynamics of any specific geothermal power plant. Coatings based on high-entropy alloys (HEA, produced by mechanical alloying and gas-atomization), cermets and Ni-P-PTFE have been deposited by means of high-velocity oxygen fuel spray (HVOF), laser cladding (LC), electrospray deposition (ESD) and electroless plating (ENP), while Ni- and Ti- based metal matrix composites (MMC) have been manufactured by means of isostatic hot pressing (HIP) and uniaxial hot pressing (UHP). Corrosion performance been determined by means of electrochemical corrosion testing, while erosion wear, erosion-corrosion wear and contact angle have been measured for the tribological performance. Cost has also been calculated in order to evaluate the potential financial benefits achieved by employing cost-effective substrates coated with the novel layer systems compared to state-of-the-art wrought alloys.

Results demonstrate that, in general, the ranking for the newly developed systems overcomes the value of state-of-the-art wrought alloys. Moreover, it is expected that the calculated ranking can be further moved in favor of the newly developed systems if they could be moved from a research to a production manufacturing framework, thus lowering the overall production costs. The two systems per application down-selected from this work are currently being tested in real geothermal conditions.

ACKNOWLEDGMENTS

This work is part of the H2020 EU project Geo-Coat: “Development of novel and cost-effective corrosion resistant coatings for high temperature geothermal applications” funded by H2020 EU project no. 764086. The authors would also like to acknowledge the resources and collaborative efforts provided by the consortium of the Geo-Coat project.

REFERENCES

- [1] S. N. Karlsdottir, "Corrosion, scaling and material selection in geothermal power production," in *Comprehensive renewable energy*, Elsevier, 2012, pp. 241-259.
- [2] J. Nogara and S. Zarrouk, "Corrosion in geothermal environment: Part 1: Fluids and their impact," *Renewable and Sustainable Energy Reviews*, vol. 82, pp. 1333-1346, 2018.
- [3] J. Nogara and S. J. Zarrouk, "Corrosion in geothermal environment Part 2: Metals and alloys," *Renewable and Sustainable Energy Reviews*, vol. 82, pp. 1347-1363, 2018.
- [4] W. Braithwaite and K. Lichti, "Surface corrosion of metals in geothermal fluids at Broadlands, New Zealand," in *Geothermal scaling and corrosion STP717*, ASTM, 1980, pp. 81-112.
- [5] J. P. Carter, F. X. McCawley, S. D. Cramer and J. P. Needham, "Corrosion Studies in Brines of the Salton Sea Geothermal Field," Avondale Metallurgy Research Center; Bureau of Mines, Washington, DC (USA), 1979.
- [6] M. T. Abisa, "Geothermal binary plant operation and maintenance systems with svartsengi power plant as a case study," *Geothermal Training Programme*, vol. 15, pp. 287-306, 2002.
- [7] F. Ravazdeh, "A study on operation and maintenance of flash steam geothermal power plants: Reykjanes power plant," UNU-GTP, Reykjavik, Iceland, 2015.
- [8] S. Thorhallsson, "Geothermal well operation and maintenance," IGC2003 - Short Course, Reykjavik, Iceland, 2003.
- [9] N. Sanada, Y. Kurata, H. Nanjo, H. Kim, J. Ikeuchi and L. KA, "IEA Deep geothermal resources subtask C: Materials progress with a database for materials performance in deep and acidic geothermal wells," in *World Geothermal Congress 2000*, Kyushu, 2000.
- [10] W. O. Jacobson, P. M. Henry, A. N. Rogers and F. Schoeflin, "Scale and corrosion parameters at a geothermal loop experimental facility," in *40th International Water Conference*, Pittsburgh, Pennsylvania, 1979.
- [11] L. E. Lorensen, C. M. Walkup and E. T. Mones, "Polymeric and composite materials for use in systems utilizing hot, flowing, geothermal brine.," in *UCRL-76855; CONF-750525-4*, California University, Livermore (USA), Lawrence Livermore Lab., 1975.
- [12] G. Allegrini and G. Benvenuti, *Personal communication to Radian Corporation*, Austin, Texas, 1979.
- [13] T. A. Maden, "Science and Technology of Surface Coatings: A NATO Advanced Study Institute," Academic Press, New York, 1972.
- [14] I. Csaki, K. R. Ragnasdottir, A. Buzaianu, K. Leosson, V. Motoiu, S. Gudlaugsson, M. V. Lungu, H. O. Haraldsdottir and S. N. Karlsdottir, "Nickel based coatings used for erosion-corrosion protection in a geothermal environment," *Surface & Coatings Technology*, vol. 350, pp. 531-541, 2018.
- [15] R. R. Reeber, "Coatings in Geothermal Energy Production," *Thin Solid Films*, vol. 72, pp. 33-47, 1980.
- [16] D. B. Miracle and O. N. Senkov, "A critical review of high entropy alloys and related concepts," *Acta Materialia*, vol. 122, pp. 448-511, 2017.
- [17] Y. Ye, Q. Wang, J. Lu, C. Liu and Y. Yang, "High-entropy alloy: challenges and prospects," *Materials Today*, vol. 19, pp. 349-362, 2016.